

# Cross-correlation of 21 cm and soft X-ray backgrounds during the epoch of reionization

Jun-Min Liang, Xiao-Chun Mao and Bo Qin

National Astronomical Observatories, Chinese Academy of Sciences, Beijing 100012, China; [liangjunmin@bao.ac.cn](mailto:liangjunmin@bao.ac.cn)

Received 2016 March 2; accepted 2016 April 25

**Abstract** The cross-correlation between the high-redshift 21 cm background and the Soft X-ray Background (SXB) of the Universe may provide an additional probe of the Epoch of Reionization. Here we use semi-numerical simulations to create 21 cm and soft X-ray intensity maps and construct their cross power spectra. Our results indicate that the cross power spectra are sensitive to the thermal and ionizing states of the intergalactic medium (IGM). The 21 cm background correlates positively to the SXB on large scales during the early stages of the reionization. However as the reionization develops, these two backgrounds turn out to be anti-correlated with each other when more than  $\sim 15\%$  of the IGM is ionized in a warm reionization scenario. The anti-correlated power reaches its maximum when the neutral fraction declines to 0.2–0.5. Hence, the trough in the cross power spectrum might be a useful tool for tracing the growth of HII regions during the middle and late stages of the reionization. We estimate the detectability of the cross power spectrum based on the abilities of the Square Kilometre Array and the *Wide Field X-ray Telescope* (WFXT), and find that to detect the cross power spectrum, the pixel noise of X-ray images has to be at least 4 orders of magnitude lower than that of the WFXT deep survey.

**Key words:** cosmic background radiation — cosmology: theory — dark ages, reionization, first stars — early Universe — diffuse radiation — X-rays: diffuse background

## 1 INTRODUCTION

Revealing the nature of the first luminous objects and their complex connection to the intergalactic medium is a major goal for our understanding of the early Universe. When the first luminous objects emerged, the ultraviolet (UV) and X-ray photons produced by these objects started to ionize their surrounding cosmic gas. Meanwhile, the energetic X-ray electrons kept heating the cosmic gas efficiently. With the formation of more and more such objects, the Universe eventually turned from cold and neutral to warm and ionized. The period during which the Universe underwent this transition is referred to as the Epoch of Reionization (EoR, see Furlanetto et al. 2006; Zaroubi 2013 for reviews). Observations of the absorption spectra of high-redshift quasars support that the Universe is highly ionized out to redshift  $z \sim 6$  (Fan et al. 2006; Bolton et al. 2011; McGreer et al. 2015). Cosmic Microwave Background (CMB) observations suggest that the reionization occurred at  $z \approx 8.8 \sim 10.1$  when an assumption of instantaneous reionization is adopted (Komatsu et al. 2011; Planck Collaboration et al. 2015), which indicates that the EoR started at higher redshifts. Nevertheless, the details of cosmic reionization are still unclear.

The redshifted 21 cm line, which is a result of the hyperfine transition in hydrogen atoms, is one of the most

promising probes of the EoR. Fluctuations in the cosmic 21 cm signals are determined by the characteristics of the coeval intergalactic medium (IGM) such as density, temperature and ionized fraction (e.g. Furlanetto et al. 2006; Pritchard & Loeb 2012). Therefore, the cosmic 21 cm background contains information on the states and distributions of the IGM. Combining with its redshift information, we can study the evolution of the IGM over time, and constrain the nature of the heating/ionizing sources as well as the structure formation processes in the early Universe. With low frequency radio interferometers such as the 21 CentiMeter Array (21CMA), the Murchison Widefield Array (MWA), the Low Frequency Array (LOFAR), the Precision Array for Probing the Epoch of Reionization (PAPER), the Giant Metrewave Radio Telescope (GMRT) and the next generation instrument – the Square Kilometre Array (SKA), we may expect to measure fluctuations in the redshifted 21 cm signal during the EoR in the near future. Recent observations with some of these interferometers have updated several constraints on the EoR (e.g. Paciga et al. 2013; Dillon et al. 2014; Parsons et al. 2014; Ali et al. 2015; Pober et al. 2015).

In addition to the 21 cm line, the soft X-ray background (SXB) can also constrain the EoR. The cosmic X-ray background was first discovered in the 1960s. Current high sensitivity X-ray telescopes such as *Chandra* and

*XMM-Newton* have resolved  $\gtrsim 90\%$  of the SXB into point and extended sources to  $z \lesssim 7$  (Moretti et al. 2003; Xue et al. 2011; Lehmer et al. 2012; Cappelluti et al. 2012). The residual fraction (unresolved SXB) is expected to be mostly due to faint extragalactic sources (AGNs and normal galaxies), which are near or below the detection limits (Bauer et al. 2004; Lehmer et al. 2012). Since the Universe and the Milky Way are transparent to  $\gtrsim 1$  keV X-ray photons (Wilms et al. 2000; Behar et al. 2011; Starling et al. 2013), hard X-ray photons with energies  $[1-2](1+z)$  keV emitted by black holes or hot IGM in the early Universe (Cappelluti et al. 2012; Pacucci et al. 2014) could be observed today in the soft X-ray band. However, most  $z \gtrsim 6$  sources are too faint to be resolved by current instruments. These source will become a component of the unresolved SXB (e.g. Salvaterra et al. 2007; McQuinn 2012; Pritchard & Loeb 2012). Mesinger et al. (2013) and Christian & Loeb (2013) have shown that the intensity of the EoR X-ray background could have a dramatic impact on the 21 cm signals and the reionization history. We may use the unresolved SXB to limit the X-ray contributions to the reionization. Recent studies (e.g. Mortlock et al. 2011; Basu-Zych et al. 2012; Venemans et al. 2013) indicate that the high-redshift components of the unresolved SXB might exist. But unfortunately, the SXB is indeed a combination of radiations from various X-ray sources at different redshifts. It is hard to obtain redshift information on the SXB itself. Currently we still do not have enough evidence of the existence of these components, and the unresolved SXB alone can only provide a few constraints on the X-ray sources at high redshifts (e.g. Dijkstra et al. 2004; McQuinn 2012).

Combining soft X-ray and low frequency radio observations might be a promising method for EoR measurement. Fluctuations in the 21 cm and X-ray backgrounds are both tracing the same underlying density field, hence the 21-SXB cross-correlation is expected to exist. Since 21 cm and X-ray backgrounds contain information on neutral gas and luminous sources respectively, their cross-correlation may provide a better tracer of the interplay between the first luminous objects and the surrounding IGM than the 21 cm or SXB auto-correlation itself does. Moreover, only the SXB components from the same redshift of the 21 cm signal will strongly correlate with the corresponding 21 cm backgrounds. We can use the 21-SXB cross-correlation signals to test the assumption that the observed unresolved SXB contains photons from the EoR. Moreover, cross-correlation is relatively insensitive to systematic effects and foreground contaminations compared to auto-correlation (Slosar et al. 2007). These properties make the 21-SXB cross power spectrum a useful tool for EoR measurements.

In this paper, we use a modified version of the semi-numerical simulations, the 21CMFAST, to investigate the evolution of the 21-SXB cross angular power spectra during the EoR. The 21-SXB cross power spectra have been studied by Shan & Qin (2009). Combining data from LOFAR and *ROSAT* in an analytic model, they

found that although the cosmic 21 cm signals could be detected, the 21-SXB power spectra are still limited by noise in the *ROSAT* surveys. Some recent ambitious proposals on new X-ray telescopes, which can conduct a wide field survey such as the *Wide Field X-ray Telescope (WFXT)* (Murray et al. 2013) and *SMART-X* (Vikhlinin & SMARTX Collaboration 2013), stimulated us to examine their performances in measurements of the 21-SXB cross power spectrum. With higher sensitivities, these X-ray telescopes are capable of achieving deeper wide field surveys than *ROSAT*, which may be promising for the detection of cross-correlation signals. Throughout the paper, we adopt the same cosmological parameters as Komatsu et al. (2011) used,  $\Omega_\Lambda = 0.73$ ,  $\Omega_M = 0.27$ ,  $\Omega_b = 0.046$ ,  $n = 0.96$ ,  $\sigma_8 = 0.82$  and  $H_0 = 70 \text{ km s}^{-1} \text{ Mpc}^{-1}$ .

## 2 METHODS

### 2.1 The 21CMFAST Simulation

We use a modified version of the 21CMFAST code to simulate the 21 cm and X-ray signals from the EoR. For more details on the original version of this simulation, see Mesinger & Furlanetto (2007), Mesinger et al. (2011) and Zahn et al. (2011).

The differential brightness temperature of the 21 cm line at an observed frequency  $\nu$  is (e.g. Furlanetto et al. 2006; Mesinger et al. 2011)

$$\begin{aligned} \delta T_b(\nu) &= \frac{T_s - T_\gamma}{1+z} (1 - e^{-\tau_{21}}) \\ &\approx 27 x_{\text{HI}} (1 + \delta) \left( \frac{H}{\frac{dv_r}{dr} + H} \right) \left( 1 - \frac{T_\gamma}{T_s} \right) \\ &\quad \times \left( \frac{1+z}{10} \frac{0.15}{\Omega_M h^2} \right)^{\frac{1}{2}} \left( \frac{\Omega_b h^2}{0.023} \right) \text{mK}, \quad (1) \end{aligned}$$

where  $T_\gamma$  is the CMB temperature,  $\delta(\mathbf{x}, z)$  is the overdensity at coordinates  $(\mathbf{x}, z)$  within the simulation volume,  $H$  is the Hubble parameter,  $dv_r/dr$  is the comoving velocity gradient in the line of sight, and  $h$  is the Hubble constant in units of  $100 \text{ km s}^{-1} \text{ Mpc}^{-1}$ . To obtain  $\delta T_b$  maps, perturbation theory and excursion-set formalism are adopted to generate density, velocity, source, ionization and spin temperature fields (Mesinger et al. 2011). A cell at  $(\mathbf{x}, z)$  is regarded as fully ionized if the criterion

$$\zeta_{\text{UV}} f_{\text{coll}} \geq 1 - x_e, \quad (2)$$

is satisfied. Here  $\zeta_{\text{UV}}$  is the ionizing efficiency parameter,  $x_e$  is the ionized fraction by X-rays and  $f_{\text{coll}}$  is the collapsed fraction describing the fraction of mass collapsed into dark matter halos with mass greater than a threshold corresponding to a mass variance,  $S_{\text{min}}$  (Mesinger et al. 2011, 2013). The mean free path of UV photons is chosen to be 40 Mpc. The collapsed fraction is given by (Barkana & Loeb 2008; Mesinger et al. 2011)

$$f_{\text{coll}}(\mathbf{x}, z, R, S_{\text{min}}) = \frac{\overline{f}_{\text{ST}}}{\overline{f}_{\text{PS}}} \text{erfc} \left[ \frac{\delta_c - \delta^R}{\sqrt{2(S_{\text{min}} - S^R)}} \right], \quad (3)$$

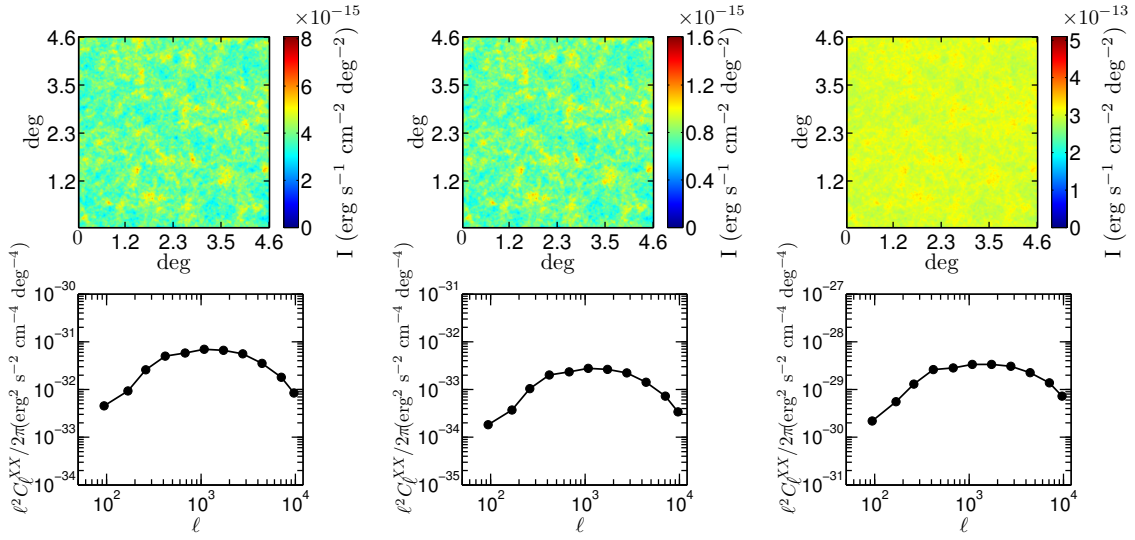


**Fig. 1** The simulated 1–2 keV X-ray maps with a field of view of about  $4.6^\circ \times 4.6^\circ$  (*upper panels*) and the corresponding soft X-ray angular power spectra (*lower panels*). The X-ray maps are generated by accumulating the X-ray radiations from sources at  $5.80 \leq z \leq 19.75$ . The left, middle and right columns are the results for fiducial, cold and extreme models, respectively.

where  $\bar{f}_{\text{ST}}/\bar{f}_{\text{PS}}$  is a normalization factor keeping the mean collapsed fraction consistent with the result of the Sheth-Tormen model (Sheth & Tormen 2002),  $\delta_c$  is the critical overdensity, and  $\delta^R(\mathbf{x}, z)$  and  $S^R$  are respectively the averaged overdensity and the relevant mass variance on a smoothed radius  $R$ .

The X-ray heating and ionizing efficiencies at  $(\mathbf{x}, z)$  depend on the intensity of the coeval X-ray background. Although we do not know the details of the X-ray sources in the early Universe, we can generally assume that the X-ray luminosity is proportional to the star formation rate (SFR, e.g. Pritchard & Loeb 2012). Thus the comoving specific X-ray emissivity of a shell surrounding the cell can be expressed as

$$\epsilon_{h_p v}(\nu_e, \mathbf{x}, z) = \alpha h_p \frac{N_X}{\mu m_p} \left( \frac{\nu_e}{\nu_0} \right)^{-\alpha} \times \left[ \rho_{\text{crit},0} \Omega_b f_* (1 + \delta^R) \frac{df_{\text{coll}}}{dt} \right], \quad (4)$$

where  $h_p$  is the Planck constant,  $\nu_e$  is the emission frequency,  $\nu_0$  is the frequency threshold beyond which the photons can penetrate into the IGM,  $N_X$  is the number of X-ray photons per stellar baryon,  $\mu m_p$  is the mean baryon mass,  $f_* = 0.1$  represents the fraction of baryons converted into stars,  $\rho_{\text{crit},0}$  is the critical density of the present-day Universe,  $\alpha$  is the spectral index and the product in the brackets is the comoving SFR density (Mesinger et al. 2013). Finally, the angle-averaged specific intensity can be computed by accumulating the X-ray photons that arrive at  $(\mathbf{x}, z)$

$$I(\nu) = \frac{(1+z)^3}{4\pi} \int \epsilon_{h_p \nu} \frac{cdt}{dz} dz. \quad (5)$$

The X-ray production efficiency is commonly parameterized by a factor,  $f_X$ . Here we define  $f_X \equiv N_X/0.12$ .

One can adjust  $f_X$  and  $\alpha$  to mimic the X-ray backgrounds resulting from different numbers and populations of the X-ray sources. Now we follow previous work (e.g. Mesinger et al. 2011, 2013) and take  $\alpha = 1.5$ . These parameters result in an X-ray luminosity,  $L_X$ , that is consistent with extrapolation from measurements of the relationship shown by nearby starburst galaxies  $L_X$ –SFR (Mineo et al. 2012; Mesinger et al. 2013, 2014).

## 2.2 The Soft X-ray Backgrounds

Most X-ray sources like starburst galaxies and mini-quasars at  $z > 6$  are however too faint to be resolved by current X-ray telescopes. These sources would produce hard X-ray photons that contribute to the present-day unresolved SXB observed by *Chandra* or *XMM-Newton* (Salvaterra et al. 2007; Pritchard & Loeb 2012; Cappelluti et al. 2012). We modify the X-ray background model in 21CMFAST to generate the EoR component of the present-day SXB. First we rewrite Equation (4) as

$$\epsilon'_{h_p v}(\nu_e, \mathbf{x}, z) = \alpha h_p \frac{N_X}{\mu m_p} \left( \frac{\nu_e}{\nu_0} \right)^{-\alpha} \times \left[ \rho_{\text{crit},0} \Omega_b f_* (1 + \delta) \frac{df'_{\text{coll}}}{dt} \right]. \quad (6)$$

This is the comoving specific X-ray emissivity of a cell at  $(\mathbf{x}, z)$ , where  $f'_{\text{coll}}$  is the global collapsed fraction at  $z$ . Then the SXB can be expressed as

$$I' = \frac{1}{4\pi} \int_{\nu_1}^{\nu_2} d\nu \int_{z_{\text{min}}}^{z_{\text{max}}} \epsilon'_{h_p \nu} \frac{cdt}{dz} dz, \quad (7)$$

where  $\nu_1$  and  $\nu_2$  respectively correspond to the lower and upper frequency limits of the observed band.

Both the IGM and the interstellar medium (ISM) in the Milky Way along the line of sight can lead to X-ray

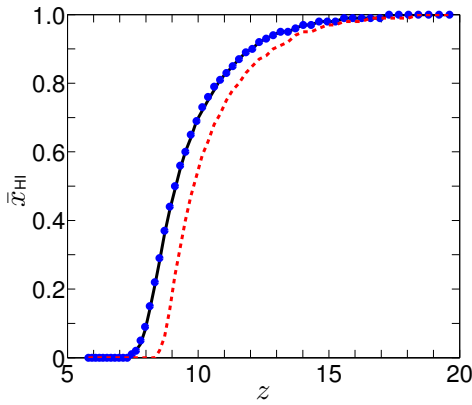


**Fig. 2** The evolution of the global neutral fraction in the fiducial (black solid line), cold (blue dotted line) and extreme (red dashed line) models.

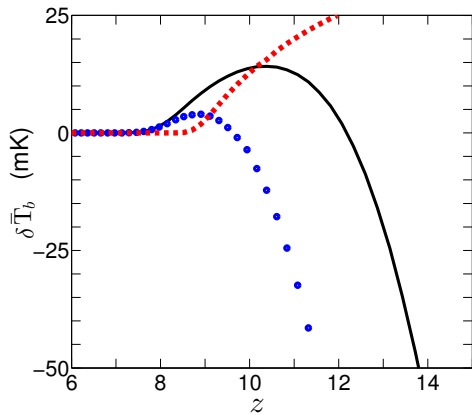


**Fig. 3** Redshift evolution of the average 21 cm differential brightness temperature for the fiducial (black solid line), cold (blue dotted line) and extreme (red dashed line) models.

absorptions. We use the results from Behar et al. (2011) and Starling et al. (2013), and assume a Galactic column density of  $10^{21} \text{ cm}^{-2}$ . The X-ray transmission at the observed energy  $E = 1 \text{ keV}$  for the EoR sources is deduced to be  $\gtrsim 0.9$  for both IGM and the local ISM. Hence, the total transmission is  $\gtrsim 0.8$  at 1 keV. The transmission will increase with  $E$ . But at  $E < 1 \text{ keV}$ , extinction becomes serious. Moreover, diffuse Galactic and local emissions dominate the SXB below 1 keV, while the extragalactic sources account for a great fraction of the unresolved 1–2 keV SXB measured by Hickox & Markevitch (2006) (see Markevitch et al. 2003; Hickox & Markevitch 2007). Therefore, we adopt the 1–2 keV band for our SXB maps, instead of the 0.5–2 keV band. The integral of redshift is realized by calculating the X-ray intensity for each cell and projecting all X-ray intensity slices of the simulation boxes between redshift  $z_{\text{min}} = 5.80$  and  $z_{\text{max}} = 19.75$  onto the sky plane. This redshift interval is wide enough to include the main part of the EoR. Here the flat-sky approximation is used for the projection.

### 2.3 The $\delta T_b$ Maps

We examine three different X-ray models, corresponding to  $f_X = 1$  (fiducial model), 0.2 (cold model) and 100 (extreme model), respectively. The upper panels of Figure 1 show the 1–2 keV soft X-ray maps for different models. These maps only display X-ray radiations from the EoR and we ignore the sources/absorbers at  $z < 5.8$  as well as the Galactic components. In addition, all these maps correspond to the same part of the sky. The intensity of the X-ray background is roughly proportional to  $f_X$ . Thus, the X-ray map in the extreme model is much brighter than that in the other two models. The average intensity of the X-ray map,  $\bar{I}'$ , is  $3.69 \times 10^{-15} \text{ erg s}^{-1} \text{ cm}^{-2} \text{ deg}^{-2}$  in the fiducial model, accounting for about 1% of the 1–2 keV unresolved SXB as estimated by Hickox & Markevitch (2007) and is under the upper limit of the very high  $z$  components given by Cappelluti et al. (2012). Although Pober et al. (2015) have ruled out the extremely cold reionization scenarios, our cold model still satisfies their constraints.

The evolutions of the global neutral fraction ( $\bar{x}_{\text{HI}}$ ) and the average differential brightness temperature ( $\delta\bar{T}_b$ ) are respectively shown in Figure 2 and Figure 3. In the extreme model, X-rays have a notable contribution to the global neutral fraction, and the efficient X-ray heating causes  $T_s \gg T_\gamma$  when the Universe was almost neutral. In the cold model, the ionization history is similar to the fiducial model (mostly driven by UV photons). But the weak X-ray background dramatically delays the heating process, leading to turnover of the 21 cm emissions ( $\delta\bar{T}_b > 0 \text{ mK}$ ) occurring much later ( $\bar{x}_{\text{HI}} \approx 0.6$ ).

Each observed frequency of the 21 cm signals corresponds to a separate redshift. Therefore, we are able to use the redshifted 21 cm backgrounds (i.e. the  $\delta T_b$  maps) at certain frequencies, which have narrow bandwidth (a slice), to correlate with the X-ray backgrounds. However, when we use a  $\delta T_b$  map to correlate with the SXB, the X-ray components at other redshifts will bring random confusing signals. Because low-redshift components dominate the X-ray backgrounds, their confusing signals may be significant for the higher redshift cross-correlations. If the bandwidths of 21 cm observations, namely the correlated redshift intervals, are too narrow, then the cross-correlation signals between the  $\delta T_b$  map and the corresponding X-ray components will be too weak to be separated from the confusing signals. Thus, we have to choose a bandwidth which is wide enough to achieve a reliable measurement but narrow enough to study the evolution of the cross power spectra during the EoR. Here, we set the bandwidth to be 6 MHz.

Our  $\delta T_b$  maps are shown in Figure 4, which are all generated by averaging slices at each frequency within the observed band. The central redshifts of these maps are  $z_{\text{mid}} = 9.2$  for the upper panels and  $z_{\text{mid}} = 12.3$  for the lower panels. For comparison, in some of these maps we mark large scale overdense/underdense regions by arrow 1 and arrow 2 respectively. The arrows with the same labels in different panels are pointing to the same position of the

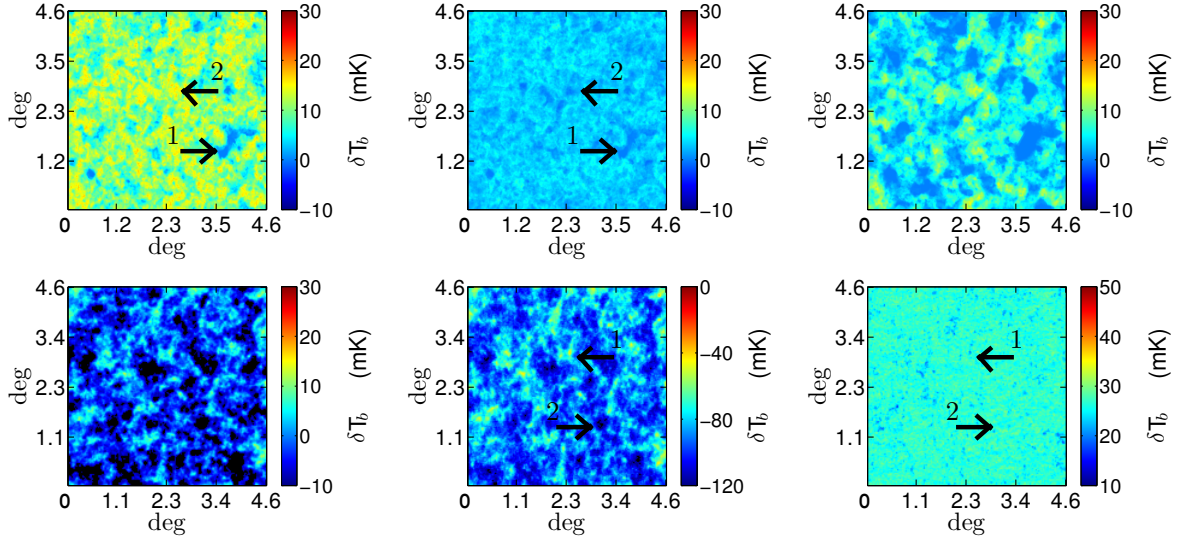


**Fig. 4** The  $4.6^\circ \times 4.6^\circ$  21 cm differential brightness temperature maps of the fiducial (left column), cold (middle column), and extreme (right column) models at  $z_{\text{mid}} = 9.2$  (upper panels) and  $12.3$  (lower panels). The bandwidth of these maps is 6 MHz.

sky plane. The first luminous objects first emerge in high density regions. In the fiducial model (left column), X-rays from these objects sufficiently heat the IGM ( $T_s > T_\gamma$ ) in overdense regions at  $z \approx 12$ . However, these objects are just beginning to ionize their surrounding IGM and create small HII regions. Hence we can find 21 cm emissions from the neutral parts of the large scale high density regions. Low SFR and long distance from galaxy clusters give rise to 21 cm absorptions in underdense regions. But as time goes on, more and more galaxies form and the IGM in low density regions becomes warm enough to emit 21 cm photons. Meanwhile, the neutral fraction of the IGM in high density regions decreases quickly with an increasing number of ionizing sources. Thus in the  $z_{\text{mid}} = 9.2$  map, the 21 cm brightness of the overdense regions is dimmer than that of the underdense regions.

As for the extreme model (right column), the high X-ray emissivity enhances the X-ray heating rate. Therefore on large scales, the IGM has been sufficiently heated to produce 21 cm emissions everywhere. The strong X-ray background also improves the X-ray ionizing rate. At  $z \approx 12.3$ , a large fraction of the IGM in the densest parts of the large scale overdense regions has already been ionized. The increase in the local ionized fraction of these areas can reduce the local differential brightness temperatures (see Eq. (1)). Therefore in the  $z_{\text{mid}} = 12.3$  map, the differential brightness temperatures of the densest regions turn out to be dimmer than those of the underdense regions which have higher neutral fraction, and the contrast between the 21 cm brightness of the overdense and underdense regions is less conspicuous on very large scales ( $\sim 30$  Mpc). We can expect that this contrast should be smaller in an earlier stage when the gas in the high density regions was less ionized. This stage, during which the 21 cm brightness temperatures in large scale high density regions decrease to roughly the same values as those in low density regions, is

referred to as the “equilibration phase” (Wyithe & Morales 2007; Lidz et al. 2009). Moreover, the  $z_{\text{mid}} = 9.2$  map of the fiducial model is brighter compared with that of the extreme model. This is because in the fiducial model the Universe has more neutral hydrogen gas at this redshift (see Fig. 2).

In the cold model (middle column), the global spin temperature keeps being lower than the CMB temperature until the middle stages of the reionization. In the  $z_{\text{mid}} = 9.2$  map, most of the neutral and partially ionized areas have begun to emit 21 cm signals. The areas marked by arrow 1 and arrow 2 both have  $\delta T_b \sim 0$  mK, indicating that the IGM is going through an equilibration phase at this redshift. In the  $z_{\text{mid}} = 12.3$  map, the differential brightness temperatures are lower than 0 mK even in the warmest regions. Note that as the neutral IGM is gradually ionized, we will find  $\delta T_b \rightarrow 0$  mK. Therefore  $\delta T_b > \delta \bar{T}_b$  even if there is no 21 cm signal. In other words, the  $\delta T_b$  field stays positively correlated with the density field when  $\delta \bar{T}_b < 0$  mK. In Section 3, we will evaluate the impact of these differences on the cross-correlation power spectra.

## 2.4 The Angular Cross Power Spectrum

To calculate the 21-SXB angular cross power spectrum, we first denote the fluctuations in 21 cm background and SXB to be  $\delta_{21} \equiv \delta T_b / \delta \bar{T}_b - 1$  and  $\delta_X \equiv I' / \bar{I}' - 1$ , respectively. Their Fourier transforms are (e.g. Morales & Hewitt 2004)

$$V_T(u, v) = \iint \delta_{21}(l, m) e^{-2\pi i(ul+vm)} dl dm, \quad (8)$$

$$V_X(u, v) = \iint \delta_X(l, m) e^{-2\pi i(ul+vm)} dl dm, \quad (9)$$

where  $l, m$  are the angular coordinates of the sky map and  $u, v$  are their corresponding Fourier transform. Then we construct the angular auto power spectra of the 21 cm and

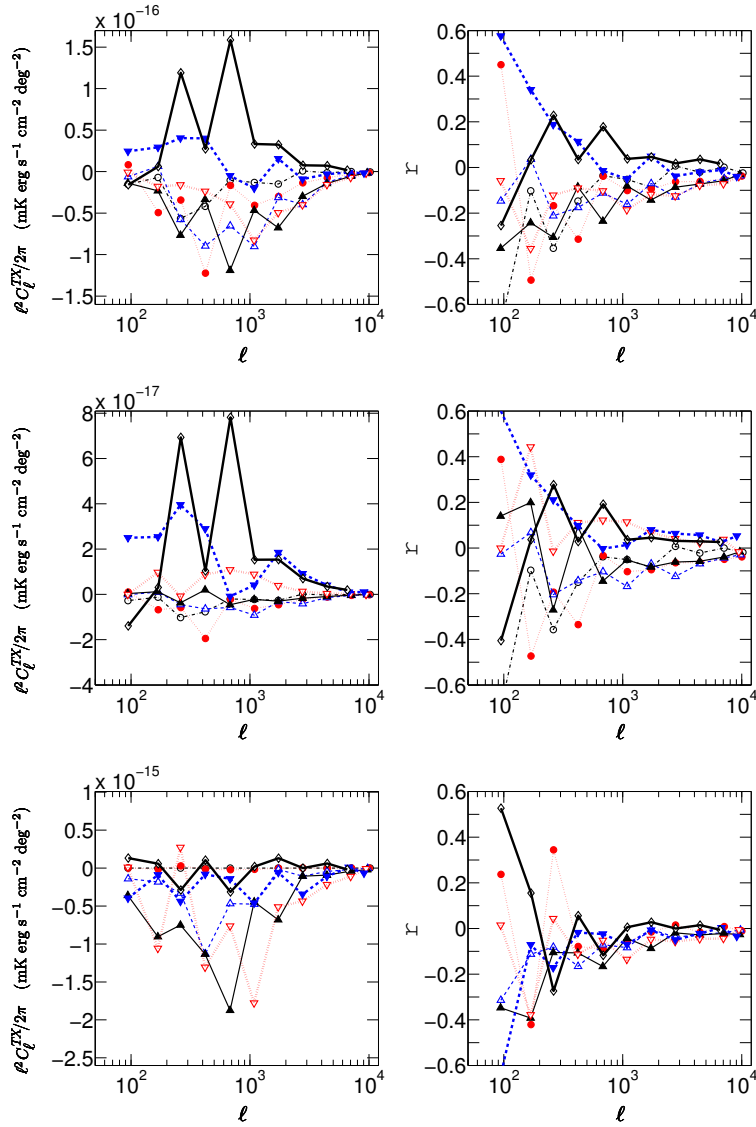


**Fig. 5** Redshift evolution of the 21-SXB cross angular power spectra (*left column*) and the corresponding correlation coefficient (*right column*) in the fiducial (*upper panels*), cold (*middle panels*) and extreme (*lower panels*) models. The black thick solid, blue thick dashed, red thick dotted, black thin solid, blue thin dashed, red thin dotted and black thin dashed lines respectively correspond to the results for  $z_{\text{mid}} = 12.3, 11.2, 9.8, 9.2, 8.8, 8.2$  and  $7.8$ .

SXB in the form given by (e.g. White et al. 1999; Datta et al. 2007; Cappelluti et al. 2013)

$$C_\ell^{\text{TT}} = \delta \bar{T}_b^2 \langle V_{\text{T}} V_{\text{T}}^* \rangle, \quad (10)$$

$$C_\ell^{\text{XX}} = \bar{I}^2 \langle V_{\text{X}} V_{\text{X}}^* \rangle, \quad (11)$$

and the angular cross power spectrum is

$$C_\ell^{\text{TX}} = \frac{\delta \bar{T}_b \bar{I}}{2} \left( \langle V_{\text{X}} V_{\text{T}}^* \rangle + \langle V_{\text{T}}^* V_{\text{X}} \rangle \right), \quad (12)$$

where  $\ell = 2\pi\sqrt{u^2 + v^2}$ . The correlation coefficient can be written as

$$r = \frac{C_\ell^{\text{TX}}}{\sqrt{C_\ell^{\text{TT}} C_\ell^{\text{XX}}}}. \quad (13)$$

## 2.5 Detectability

We express the errors of a measurement of auto angular power spectra as (Knox 1995; Mao 2014)

$$\Delta C_\ell^{ii} = \sqrt{\frac{2}{N}} [C_\ell^{ii} + N_\ell^{ii}], \quad (14)$$

where  $i = \text{X}$  and  $\text{T}$  correspond to the result of the X-ray and 21 cm measurements respectively,  $N$  is the number of the sample within the  $\ell$  mode bin, and  $N_\ell^{ii}$  is the instrumental noise

$$N_\ell^{ii} = \sigma_i^2 \Omega_{\text{pix}} \theta_b^{2\ell(\ell+1)}, \quad (15)$$

where  $\sigma_i$  is the pixel noise,  $\Omega_{\text{pix}} = \theta_{\text{FWHM}} \times \theta_{\text{FWHM}}$  is the pixel solid angle,  $\theta_{\text{FWHM}}$  is the full width at half maximum (FWHM) of the experimental beam, and  $\theta_b$  is the beam

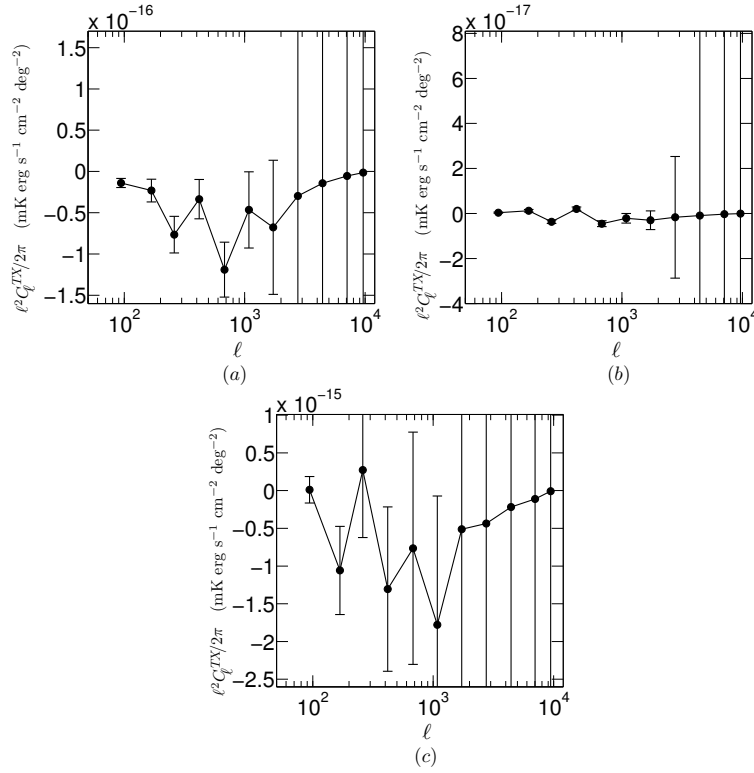


**Fig. 6** The 21-SXB cross angular power spectra with errors at  $\bar{x}_{\text{HI}} \approx 0.5$ . Panels (a), (b) and (c) correspond to the fiducial, cold and extreme models, respectively, after improving the sensitivity of the X-ray telescope.

width. Assuming that the beam is Gaussian, we have

$$\theta_b = (8 \lg 2)^{-1/2} \theta_{\text{FWHM}}. \quad (16)$$

The errors in the cross-correlation measurement can be written as

$$\begin{aligned} \Delta C_\ell^{\text{TX}} &= \sqrt{\frac{1}{N} \left[ (C_\ell^{\text{TX}})^2 + (C_\ell^{\text{TT}} + N_\ell^{\text{TT}})(C_\ell^{\text{XX}} + N_\ell^{\text{XX}}) \right]^{1/2}} \\ &= \sqrt{\frac{1}{N} \left[ (C_\ell^{\text{TX}})^2 + C_\ell^{\text{TT}} C_\ell^{\text{XX}} + N_\ell^{\text{TT}} C_\ell^{\text{XX}} \right.} \\ &\quad \left. + C_\ell^{\text{TT}} N_\ell^{\text{XX}} + N_\ell^{\text{TT}} N_\ell^{\text{XX}} \right]^{1/2}}. \end{aligned} \quad (17)$$

The foreground effects are ignored for both 21 cm and X-ray observations. With the core of the SKA1<sup>1</sup>, the pixel size of the 21 cm maps is  $\sim 1$  arcmin. We assume an integration time of 1000 hours and take  $\sigma_{\text{T}} = 1$  mK (Mellema et al. 2013). As for X-ray measurements, considering that both the *WFXT* and *SMART-X* have the goal of performing a wide field survey with the same field depth as *Chandra*, and that the sensitivity of *eROSITA* is lower than that of *WFXT* (Murray et al. 2013), we adopt the parameters of the *WFXT* deep survey (Tozzi et al. 2011; Murray et al. 2013) for the calculation. This planned X-ray telescope has a FWHM of 5 arcsec and its deep survey has a 100 square degree field of view with a 400 ks exposure.

We calculate the pixel noise by (Li & Ma 1983; Tozzi et al. 2011)

$$\text{CTN} = \text{BCK}_{\text{rate}} \times T_{\text{exp}} \times \Omega_{\text{pix}}, \quad (18)$$

and

$$\sigma_{\text{X}} = \frac{\text{ECF}}{\Omega_{\text{pix}} T_{\text{exp}}} \sqrt{\text{CTN}}, \quad (19)$$

where CTN is the instrumental background (particle background) count in a pixel after a  $T_{\text{exp}} = 400$  ks exposure,  $\text{BCK}_{\text{rate}}$  is the background photon rate, and ECF is the energy conversion factor.  $\text{BCK}_{\text{rate}} = 0.188 \text{ cts s}^{-1} \text{ deg}^{-2}$  and  $\text{ECF} = 2.25 \times 10^{-13} \text{ erg s}^{-1} \text{ cm}^{-2} / (\text{cts s}^{-1})$  for the 0.5–2 keV band are taken from Tozzi et al. (2011). We recalculate their corresponding values for the 1–2 keV band to estimate  $\sigma_{\text{X}}$ . The soft X-ray auto power spectra are shown in the lower panels of Figure 1. In the extreme model,  $\Delta C_\ell^{\text{XX}} / C_\ell^{\text{XX}} \sim 10^4$  at  $\ell \lesssim 1000$ , and the signal to noise values are much lower in the fiducial and cold models.

### 3 RESULTS

We now illustrate the evolution of the 21-SXB cross angular power spectra during the EoR. Figure 5 shows the cross angular power spectra and their corresponding correlation coefficients. The bin width is chosen to be  $\Delta\ell/\ell = 0.6$ .

It can be seen that the 21 cm backgrounds and the SXBs are positively correlated with each other at high redshifts and become anti-correlated at lower redshifts. The

<sup>1</sup> [www.skatelescope.org](http://www.skatelescope.org)

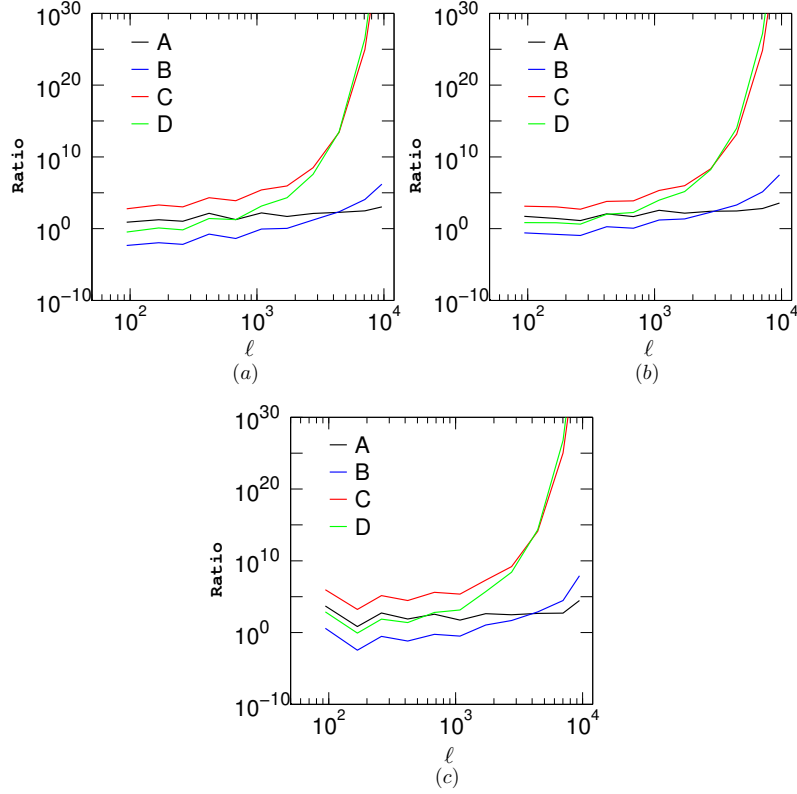


**Fig. 7** The relative strengths of diverse noise components for the  $\bar{x}_{\text{HI}} \approx 0.5$  noise reduced cross power spectra. Panels (a), (b) and (c) correspond to the fiducial, cold and extreme models, respectively. Definitions of terms A to D are given by Eq. (20).

interior of the bubble is ionized independently from the local source field. Hence, as the bubble grows, we can roughly find that the anti-correlation first becomes weak on small scales, then on larger scales. The cross power spectra may provide us more information. During the early stages of the EoR, the large scale overdense regions have higher 21 cm brightness temperatures and appear brighter in X-rays than the large scale underdense regions. Therefore in all of the three models, the 21 cm backgrounds are positively correlated with the 1–2 keV X-ray maps. However, a turnover from positive correlation to anti-correlation occurs with time. This transition corresponds to the equilibration phase, which we have mentioned in Section 2.3. In our fiducial (Fig. 5, upper panels) and extreme models (Fig. 5, lower panels), this phase occurs when  $\bar{x}_{\text{HI}} \approx 0.8$  to 0.9.

The 21 cm and SXB backgrounds become anti-correlated after the equilibration phase. The crossover scale mentioned by Shan & Qin (2009), corresponding to the characteristic bubble size, is indistinct in all of our models. But we can find a marked trough in the power spectrum after the equilibration phase in the fiducial model. The trough first emerges on small scales and shifts to large scales as reionization proceeds, representing the growth of characteristic bubble size. The amplitude of the trough reaches a maximum when 20% to 50% of the HI gas is ionized ( $z \approx 8.2$  to 9.2). Then the strength of the cross power spectrum quickly falls when  $\bar{x}_{\text{HI}} \lesssim 0.2$ .

Finally, the 21 cm background and SXBs turn out to be uncorrelated with the Universe being fully ionized.

In the extreme model (Fig. 5, lower panels), evolution of the 21-SXB cross angular power spectrum is similar to the case in the fiducial model. However, strong X-ray radiations provide more heating and ionization. Compared to the case of the fiducial model, the positive correlation appears at higher redshifts ( $z > 13$ ), and the reionization ends earlier. The correlation coefficient at  $z = 7.8$  is not given here since a fully ionized Universe no longer has 21 cm signals on large scales.

In the cold model (Fig. 5, middle panel), the period of positive 21-SXB correlation is much longer than that in the fiducial model since the cold IGM maintains the positive correlation between the  $\delta T_{\text{b}}$  and density fields. The anti-correlation between the 21 cm and SXB will not emerge until the average spin temperature reaches or exceeds the CMB temperature (i.e.  $\delta \bar{T}_{\text{b}} > 0$ ) to ensure  $\delta T_{\text{b}} - \delta \bar{T}_{\text{b}} < 0$  for the highly ionized regions and  $\delta T_{\text{b}} - \delta \bar{T}_{\text{b}} > 0$  for the highly neutral regions. In this situation, the transition from positive- to anti-correlation acts more as an indicator of the IGM thermal state, rather than as a measure of the global ionized fraction. As we see in Figure 5, the trough of the  $z_{\text{mid}} = 9.2$  power spectrum is not clear because the equilibration phase has not completed at this redshift ( $\bar{x}_{\text{HI}} \approx 0.5$ ), and the trough has not reached the maximum at  $z \approx 8.8$  ( $\bar{x}_{\text{HI}} \approx 0.4$ ). After the IGM is adequately

heated, the negative trough shifts, as we see in the other two models. This may help us to study the growth of the bubbles.

The measurement errors in the cross power spectrum are 4 orders of magnitude higher than the signal at  $\ell \approx 1100$  in the extreme model. For the fiducial and cold models, the results are 1–2 orders of magnitude worse than the extreme one. The measurement uncertainties are dominated by the instrumental noise of the *WFXT*. We extend the sky coverage fraction of the surveys to 25%, and increase the exposure of the X-ray observation to 4 Ms. To achieve a significant detection of the large scale 21-SXB cross power spectra at  $\bar{x}_{\text{HI}} \approx 0.5$ , the X-ray image pixel noise has to be further lowered by at least 1 order of magnitude for the extreme model, and by about 3–4 orders of magnitude for the fiducial and cold models. The  $\bar{x}_{\text{HI}} \approx 0.5$  cross power spectra after the noise reduction are shown in Figure 6 and the related noise analyses are shown in Figure 7. We define terms A–D to be (see Eq. (17))

$$\begin{aligned} A &= C_{\ell}^{\text{TT}} C_{\ell}^{\text{XX}} / (C_{\ell}^{\text{TX}})^2, \\ B &= N_{\ell}^{\text{TT}} C_{\ell}^{\text{XX}} / (C_{\ell}^{\text{TX}})^2, \\ C &= C_{\ell}^{\text{TT}} N_{\ell}^{\text{XX}} / (C_{\ell}^{\text{TX}})^2, \\ D &= N_{\ell}^{\text{TT}} N_{\ell}^{\text{XX}} / (C_{\ell}^{\text{TX}})^2. \end{aligned} \quad (20)$$

In all the models, the C term dominates the measurement uncertainty at  $\ell \lesssim 3000$ , indicating that the X-ray instrumental noise is still the most significant component of the errors on these scales. At  $\ell \gtrsim 3000$ , the errors are mostly caused by the instrumental noises of the X-ray and 21 cm measurements. Considering that none of the existing or currently planned X-ray telescopes could possibly reach these sensitivity requirements, it will still be difficult to detect the 21-SXB cross power spectra in the near future.

## 4 DISCUSSION

A synergy of X-ray and 21 cm observations may provide us with additional information about the details of the EoR, compared with pure 21 cm observations, as we have demonstrated in the paper. We use semi-numerical simulations to generate the cosmic 21 cm and 1–2 keV X-ray backgrounds, and then investigate the evolution of cross power spectra between these two intensity maps.

The strength of the coeval X-ray background may significantly affect the thermal and ionizing states of the IGM at high redshifts, leaving an imprint on the 21-SXB cross power spectra. On large scales, the 21 cm emission positively correlates with the SXB when  $\bar{x}_{\text{HI}} \gtrsim 0.9$ . If the X-ray heating is efficient enough to ensure  $\delta\bar{T}_{\text{b}} > 0$  mK before the IGM in large scale overdense regions are remarkably ionized, then the cross-correlation will turn out to be anti-correlated when  $\bar{x}_{\text{HI}} \approx 0.8 - 0.9$ . Otherwise, the transition of correlation will not occur until the average spin temperature exceeds the CMB temperature. Sometimes, we find strong anti-correlation at  $\ell \lesssim 200$  when the Universe is almost neutral. This is because samples within these  $\ell$  bins are extremely insufficient, lead-

ing the expectations of the cross power spectrum on these scales to be imprecise. After the transition, we can find a distinct trough in the cross power spectrum. This trough shifts from large to small  $\ell$  as the characteristic bubble size grows. In the warm reionization scenarios, the amplitude of the negative trough becomes highest when  $\bar{x}_{\text{HI}} \approx 0.2-0.5$ , then it gradually falls to zero when  $\bar{x}_{\text{HI}} < 0.2$ . With these properties, the 21-SXB cross power spectra can constrain the evolution histories of the global neutral fraction and the IGM temperature, as well as the intensity of the coeval X-ray background during the EoR. In addition, if we successfully detect the unique anti-correlation, we can verify the existence of the EoR components in the present-day unresolved SXB.

Unfortunately, the instrumental noise of the *WFXT* is too high and the 21-SXB cross power spectrum is well below the detection limit, though among all the existing designs of wide field X-ray telescopes (e.g. Merloni et al. 2012; Murray et al. 2013; Vikhlinin & SMARTX Collaboration 2013), the *WFXT* is one of the best candidates which has sufficient sensitivity to survey at the same deep depth as *Chandra*. Therefore, a detection of the 21-SXB cross power spectra in the near future is unlikely. As shown in Figure 6, for a typical EoR X-ray background (i.e. our fiducial model) to achieve a significant detection of the 21-SXB cross power spectra, the pixel noise of the X-ray measurement has to be at least 4 orders of magnitude lower than that of the *WFXT* deep survey. This is a great challenge for the designs of future X-ray telescopes.

**Acknowledgements** We thank Xiang-Ping Wu, Andrei Mesinger and Huan-Yuan Shan for helpful discussions. We are grateful to an anonymous referee for comments. This work was supported by the National Natural Science Foundation of China (Grant Nos.11473031, 11261140641 and 11173028) and the 973 Program (Grant No. 2013CB837900).

## References

- Ali, Z. S., Parsons, A. R., Zheng, H., et al. 2015, *ApJ*, 809, 61
- Barkana, R., & Loeb, A. 2008, *MNRAS*, 384, 1069
- Basu-Zych, A., Lehmer, B., Hornschemeier, A., et al. 2012, in *American Astronomical Society Meeting Abstracts*, 219, 111.07
- Bauer, F. E., Alexander, D. M., Brandt, W. N., et al. 2004, *AJ*, 128, 2048
- Behar, E., Dado, S., Dar, A., & Laor, A. 2011, *ApJ*, 734, 26
- Bolton, J. S., Haehnelt, M. G., Warren, S. J., et al. 2011, *MNRAS*, 416, L70
- Cappelluti, N., Ranalli, P., Roncarelli, M., et al. 2012, *MNRAS*, 427, 651
- Cappelluti, N., Kashlinsky, A., Arendt, R. G., et al. 2013, *ApJ*, 769, 68
- Christian, P., & Loeb, A. 2013, *J. Cosmol. Astropart. Phys.*, 9, 014

- Datta, K. K., Choudhury, T. R., & Bharadwaj, S. 2007, *MNRAS*, 378, 119
- Dijkstra, M., Haiman, Z., & Loeb, A. 2004, *ApJ*, 613, 646
- Dillon, J. S., Liu, A., Williams, C. L., et al. 2014, *Phys. Rev. D*, 89, 023002
- Fan, X., Strauss, M. A., Richards, G. T., et al. 2006, *AJ*, 131, 1203
- Furlanetto, S. R., Oh, S. P., & Briggs, F. H. 2006, *Phys. Rep.*, 433, 181
- Hickox, R. C., & Markevitch, M. 2006, *ApJ*, 645, 95
- Hickox, R. C., & Markevitch, M. 2007, *ApJ*, 661, L117
- Knox, L. 1995, *Phys. Rev. D*, 52, 4307
- Komatsu, E., Smith, K. M., Dunkley, J., et al. 2011, *ApJS*, 192, 18
- Lehmer, B. D., Xue, Y. Q., Brandt, W. N., et al. 2012, *ApJ*, 752, 46
- Li, T.-P., & Ma, Y.-Q. 1983, *ApJ*, 272, 317
- Lidz, A., Zahn, O., Furlanetto, S. R., et al. 2009, *ApJ*, 690, 252
- Mao, X.-C. 2014, *ApJ*, 790, 148
- Markevitch, M., Bautz, M. W., Biller, B., et al. 2003, *ApJ*, 583, 70
- McGreer, I. D., Mesinger, A., & D’Odorico, V. 2015, *MNRAS*, 447, 499
- McQuinn, M. 2012, *MNRAS*, 426, 1349
- Mellema, G., Koopmans, L. V. E., Abdalla, F. A., et al. 2013, *Experimental Astronomy*, 36, 235
- Merloni, A., Predehl, P., Becker, W., et al. 2012, arXiv:1209.3114
- Mesinger, A., & Furlanetto, S. 2007, *ApJ*, 669, 663
- Mesinger, A., Furlanetto, S., & Cen, R. 2011, *MNRAS*, 411, 955
- Mesinger, A., Ferrara, A., & Spiegel, D. S. 2013, *MNRAS*, 431, 621
- Mesinger, A., Ewall-Wice, A., & Hewitt, J. 2014, *MNRAS*, 439, 3262
- Mineo, S., Gilfanov, M., & Sunyaev, R. 2012, *MNRAS*, 419, 2095
- Morales, M. F., & Hewitt, J. 2004, *ApJ*, 615, 7
- Moretti, A., Campana, S., Lazzati, D., & Tagliaferri, G. 2003, *ApJ*, 588, 696
- Mortlock, D., Warren, S., Patel, M., et al. 2011, in *Galaxy Formation*, 88
- Murray, S. S., Borgani, S., Campana, S., et al. 2013, *Mem. Soc. Astron. Italiana*, 84, 790
- Paciga, G., Albert, J. G., Bandura, K., et al. 2013, *MNRAS*, 433, 639
- Pacucci, F., Mesinger, A., Mineo, S., & Ferrara, A. 2014, *MNRAS*, 443, 678
- Parsons, A. R., Liu, A., Aguirre, J. E., et al. 2014, *ApJ*, 788, 106
- Planck Collaboration, Ade, P. A. R., Aghanim, N., et al. 2015, arXiv:1502.01589
- Pober, J. C., Ali, Z. S., Parsons, A. R., et al. 2015, *ApJ*, 809, 62
- Pritchard, J. R., & Loeb, A. 2012, *Reports on Progress in Physics*, 75, 086901
- Salvaterra, R., Haardt, F., & Volonteri, M. 2007, *MNRAS*, 374, 761
- Shan, H.-Y., & Qin, B. 2009, *RAA (Research in Astronomy and Astrophysics)*, 9, 73
- Sheth, R. K., & Tormen, G. 2002, *MNRAS*, 329, 61
- Slosar, A., Cooray, A., & Silk, J. I. 2007, *MNRAS*, 377, 168
- Starling, R. L. C., Willingale, R., Tanvir, N. R., et al. 2013, *MNRAS*, 431, 3159
- Tozzi, P., Santos, J., Yu, H., et al. 2011, *Memorie della Societa Astronomica Italiana Supplementi*, 17, 24
- Venemans, B. P., Findlay, J. R., Sutherland, W. J., et al. 2013, *ApJ*, 779, 24
- Vikhlinin, A., & SMARTX Collaboration. 2013, *Mem. Soc. Astron. Italiana*, 84, 805
- White, M., Carlstrom, J. E., Dragovan, M., & Holzappel, W. L. 1999, *ApJ*, 514, 12
- Wilms, J., Allen, A., & McCray, R. 2000, *ApJ*, 542, 914
- Wyithe, J. S. B., & Morales, M. F. 2007, *MNRAS*, 379, 1647
- Xue, Y. Q., Luo, B., Brandt, W. N., et al. 2011, *ApJS*, 195, 10
- Zahn, O., Mesinger, A., McQuinn, M., et al. 2011, *MNRAS*, 414, 727
- Zaroubi, S. 2013, in *Astrophysics and Space Science Library*, 396, *The First Galaxies*, eds. T. Wiklind, B. Mobasher, & V. Bromm, 45